

## GENETICS

# Genome-editing prodrug: Targeted delivery and conditional stabilization of CRISPR-Cas9 for precision therapy of inflammatory disease

Xiaojie Yan<sup>1†</sup>, Qi Pan<sup>1†</sup>, Huhu Xin<sup>1</sup>, Yuxuan Chen<sup>1</sup>, Yuan Ping<sup>1,2\*</sup>

Regulation of CRISPR-Cas9 functions *in vivo* is conducive to developing precise therapeutic genome editing. Here, we report a CRISPR-Cas9 prodrug nanosystem (termed NanoProCas9), which combines the targeted delivery and the conditional activation of CRISPR-Cas9 for the precision therapy of inflammatory bowel disease. NanoProCas9 is composed of (i) cationic poly( $\beta$ -amino ester) (PBAE) capable of complexing plasmid DNA encoding destabilized Cas9 (dsCas9) nuclease, (ii) a layer of biomimetic cell membrane coated on PBAE/plasmid nanocomplexes for the targeted delivery of PBAE/dsCas9 complexes, and (iii) the stimuli-responsive precursory molecules anchored on the exofacial membrane. The systemic administration of NanoProCas9 enables the targeted delivery of dsCas9 plasmid into inflammatory lesions, where the precursory small molecule can be activated by ROS signals to stabilize expressed dsCas9, thereby activating Cas9 function for inflammatory genome editing. The proposed “genome-editing prodrug” presents a proof-of-concept example to precisely regulate CRISPR-Cas9 functions by virtue of particular pathological stimuli *in vivo*.

## INTRODUCTION

The genome engineering by virtue of RNA-guided endonuclease from bacterial clustered, regularly interspaced, short palindromic repeats (CRISPR)–associated protein 9 (Cas9) represents a facile, powerful tool to edit genome with high specificity. CRISPR-Cas9–based genome-editing technologies hold enormous potentials for a wide range of applications across basic science, medicine, and biotechnology. Particularly, genome editing with CRISPR-Cas9 has shown great therapeutic benefits for the treatment of genetic disorders, such as Duchenne muscular dystrophy syndrome (1) and  $\beta$ -haemoglobinopathies (2). Besides, CRISPR-Cas9–based therapeutic genome editing is also emerging as a potential option for the remission or the treatment of intractable inflammatory diseases (3–5). As a constitutive active form, wild-type Cas9 nuclease is often used for therapeutic genome editing *in vivo*; however, the nonspecific distribution of Cas9 raises safe concerns as a result of off-target activity at the tissue level. For example, adeno-associated virus–mediated delivery of CRISPR-Cas9 has shown accumulation in the nonspecific organs such as liver, heart, brain, and muscle, which remains a major concern of genotoxicity (6). To this end, recent efforts have been dedicated to developing optical strategies to improve spatial specificity by regulating Cas9 activity in response to light irradiation *in vivo* (7, 8). Although the regulation of Cas9 functions by light presents several distinctive features, such as non-invasiveness and reversibility (9), the manipulation modality suffers from the penetration depth of light when it comes to *in vivo* investigations, a major barrier impeding genome editing at deep tissues or organs (10).

Recent advances in chemical control to modulate Cas9 functions by small molecules open new avenues to regulate Cas9 activity at

both transcriptional and posttranscriptional levels. In general, chemical control of Cas9 functions takes advantages of the ability of tailored small molecules to activate or inhibit Cas9 nuclease activity. Several chemical control strategies, such as destabilized Cas9 (dsCas9) systems (11, 12), self-splicing intein-Cas9 systems (13), and dimerization of split-Cas9 systems (14), have been designed in an attempt to increase spatiotemporal specificity of CRISPR-Cas9 genome editing. As opposed to light, small molecules can be ideally delivered in an organ-specific manner to reach the deep tissues from the site of administration, eliminating the critical issue of penetration depth that optical regulation suffers (15). However, the precise regulation of Cas9 activities across temporal and spatial dimensions by small molecules has yet to be demonstrated *in vivo* and remains to be elusive due to the following reasons. First, only both small-molecule modulators and conditional CRISPR-Cas9 systems that reach the target tissue simultaneously can recover the activity of CRISPR-Cas9 for the targeted genome editing. Second, although the targeted delivery could improve the accumulation of both cargoes in the target organs, the nonspecific distribution and activation of CRISPR-Cas9, caused by the inherent leakage of cargoes during the delivery processes, are still unavoidable. Third, to be effective, both cargoes should be coloaded into a single delivery vector to amplify the activity and the therapeutic effects of CRISPR-Cas9.

To address the above issues, we here present the first site-specific, activatable CRISPR-Cas9 nanoprodrug system (termed NanoProCas9), which combines the targeted delivery and the conditional activation of CRISPR-Cas9 in response to particular biological signals *in vivo*. NanoProCas9 is designed as follows (Fig. 1A). First, poly( $\beta$ -amino ester) (PBAE), a cationic polymer capable of delivering nucleic acids efficiently (16, 17), was used to deliver plasmid DNA encoding dsCas9 with dihydrofolate reductase (DHFR) domains (12). Subsequently, a layer of biomimetic macrophage membrane (MM) is exploited to coat on the PBAE/plasmid nanocomplex surface to afford the targeted delivery of dsCas9 to the inflammatory lesions. Last, a reactive oxygen species (ROS)–responsive, precursory molecule (termed BAM-TK-TMP) with the hydrophobic tail is anchored

Copyright © 2021  
The Authors, some  
rights reserved;  
exclusive licensee  
American Association  
for the Advancement  
of Science. No claim to  
original U.S. Government  
Works. Distributed  
under a Creative  
Commons Attribution  
NonCommercial  
License 4.0 (CC BY-NC).

<sup>1</sup>College of Pharmaceutical Sciences, Zhejiang University, Hangzhou 310058, China.

<sup>2</sup>Liangzhu Laboratory, Zhejiang University Medical Center, 1369 West Wenyi Road, Hangzhou 311121, China.

\*Corresponding author. Email: pingy@zju.edu.cn

†These authors contributed equally to this work.

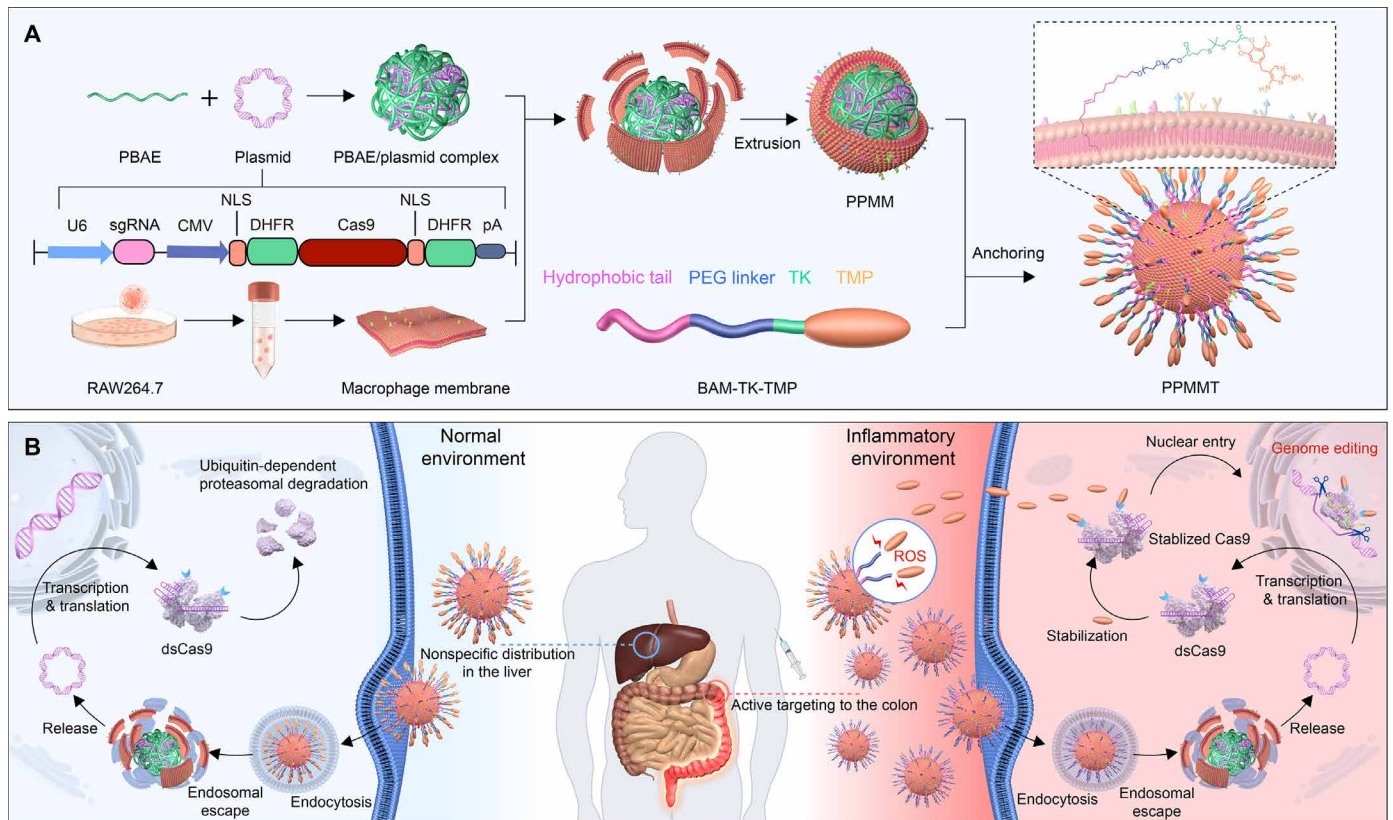


**Fig. 1. Schematic illustration of targeted delivery and inflammation-specific genome editing mediated by NanoProCas9 system.** (A) Process of preparation of the PPMMT complex. The plasmid encoding the dsCas9 sequence with DHFR domains is first designed and is then complexed with the cationic polymer (PBAE) to form PBAE/plasmid complexes. Afterward, the polyplexes are coated with MMs derived from RAW264.7 cells by extrusion to obtain membrane-coated polyplexes (PPMM). Last, a small-molecule stabilizer (TMP) for dsCas9 was covalently conjugated to OE-PEG through a thioketal linker to obtain ROS-responsive BAM-TK-TMP, which was further anchored on the membrane of PPMM to obtain PPMMT. CMV, cytomegalovirus. (B) Illustration of targeted delivery and inflammation-specific genome editing in the inflammatory colon lesion. PPMMT can preferably target the inflammatory colons by virtue of MMs, on which anchored TMP can be released accompanied by the cleavage of thioketal linker mediated in the inflammatory environment. Thus, the plasmid delivered by PPMMT can be translated into dsCas9 and stabilized upon the released TMP to recover the genome-editing activity. However, the translated dsCas9 is subjected to ubiquitin-dependent proteasomal degradation in the noninflammatory tissues, thereby minimizing off-target genome editing at the tissue level despite the nonspecific distribution of PPMMT nanoassemblies.

on the macrophage exofacial membrane through lipid fusion. As shown in Fig. 1B, after the systemic administration of NanoProCas9, the biomimetic MM can direct NanoProCas9 to the inflammatory lesion, where the small molecule can be activated by ROS signals to release its active form, trimethoprim (TMP). Therefore, the expressed dsCas9 only becomes stabilized in the presence of TMP and exerts its genome-editing missions for the modification of target genome loci. Nevertheless, in the presence of inactive BAM-TK-TMP or in the absence of TMP, structurally unstable dsCas9 is quickly subjected to the ubiquitin-dependent proteasomal degradation (18), thereby losing its nuclease activity to edit the target genome loci. It should be noted that when the ROS level becomes normal after the therapy, the administration of NanoProCas9 may not induce editing. As the TMP is readily to be customized to respond to other pathological and physiological signals like adenosine 5'-triphosphate (ATP) (19), redox (20, 21), pH (22), and enzymes (23), such a system represents an appealing platform for both efficient delivery and targeted activation of CRISPR-Cas9 in response to particular pathological signals for precision genome editing *in vivo*.

## RESULTS

### Characterization of NanoProCas9

Here, we developed a biomimetic nanoassembly composed of PBAE with the ability to complex the plasmid encoding dsCas9 and single-guide RNA (sgRNA), a layer of MM with the capability of actively targeting inflammatory lesions, and the small molecules stabilizing dsCas9 in the environment of demand. The illustration of assembly process of NanoProCas9 was shown in Fig. 1A. First, PBAE, a cationic polymer that has previously shown to efficiently deliver plasmid DNA (16, 17, 24), was synthesized (figs. S1 to S4) and used to complex plasmid encoding dsCas9 to form nanoscale polyplexes (termed NP). Second, the MM was extracted by repeated freeze-thaw in the liquid nitrogen and was further coated on polyplexes after the extrusion (termed PPMM) (25, 26). The morphology and size distribution of obtained MM, NP, and PPMM were characterized by transmission electron microscopy (TEM) and dynamic light scattering (DLS), respectively. As shown in Fig. 2A, MM formed typical hollow-structured vesicles with a thickness of approximately 10 nm, and DLS analysis indicated the irregular distribution of MM due to their nature of fragments. At the N/P ratio of 4:1, NP

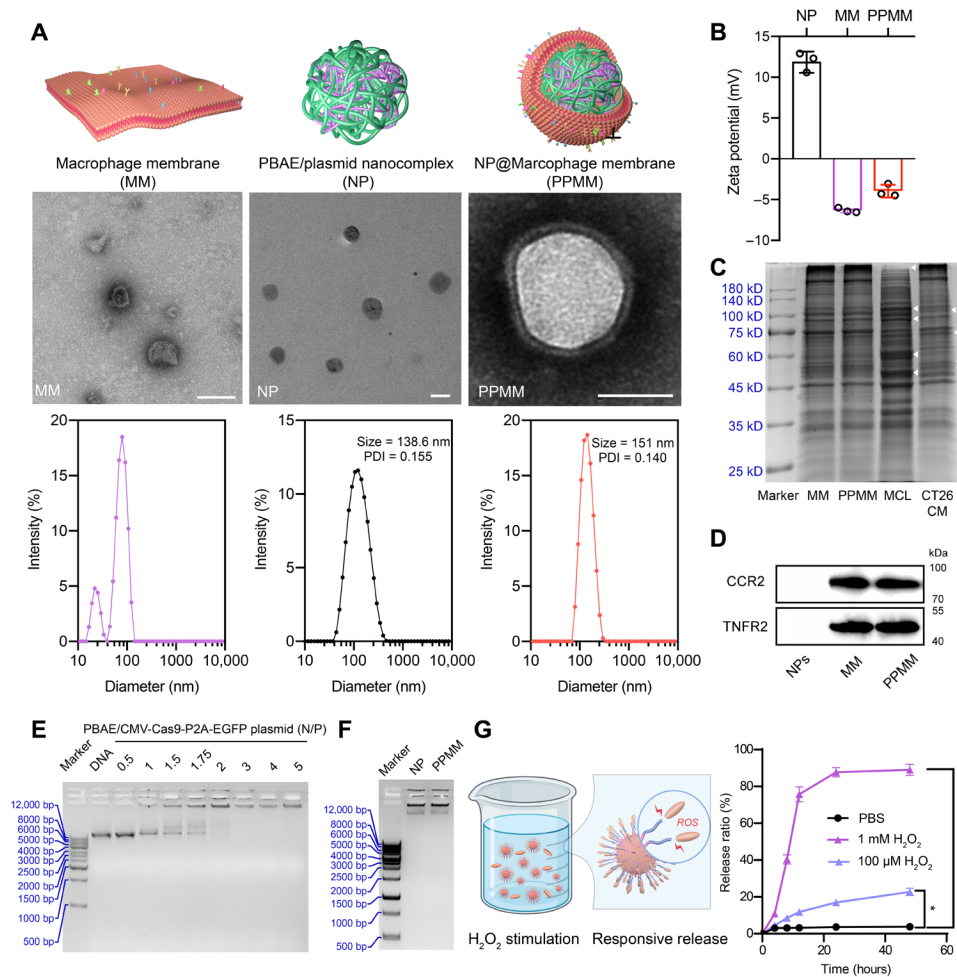


**Fig. 2. Characterization of MM-coated nanoassemblies and evaluation of ROS responsiveness of PPMMT.** (A) Schematic illustration (top), representative TEM images (middle), and size distribution (bottom) of macrophage membrane vesicle (MM), PBAE/plasmid complex (NP), and macrophage membrane-coated NP (PPMM). MM and PPMM were negatively stained with phosphotungstic acid and were subsequently visualized with TEM. Scale bar, 100 nm. PDI, polydispersity index. (B) Zeta potential analysis of NP, MM, and PPMM. Means  $\pm$  SD ( $n = 3$ ). (C) SDS-polyacrylamide gel electrophoresis (SDS-PAGE) analysis of proteins of MM, PPMM, macrophage cell lysate (MCL; cytosol proteins), and cell membrane of CT26 (CT26 CM). White arrows indicate the differences of protein profiles among the MCL, CT26 CM, and PPMM. (D) Western blotting analysis of cell membrane proteins of NP, MM, and PPMM. (E) DNA gel retardation experiments of naked DNA, PBAE/CMV-Cas9-P2A-EGFP at various N/P ratios, and NP and PPMM nanoassemblies at an N/P ratio of 4. (F) The N/P value was calculated as the ratio of positively charged amines within PBAE to negatively charged phosphorus groups in the plasmid DNA. (G) Release profiles of TMP from BAM-TK-TMP anchored on the cell membranes in the presence of 100  $\mu$ M or 1 mM  $H_2O_2$ . The released TMP was quantified by ultraviolet-visible spectroscopy (UV-Vis). The data represent means  $\pm$  SD ( $n = 3$ ). One-way ANOVA with a Tukey post hoc test, \* $P < 0.05$  and \*\*\*\* $P < 0.0001$ . PBS, phosphate-buffered saline.

displayed an average size of 138.6 nm, presenting spherical shape and relatively compact structure. After coating with the MM, a thin layer of coating shell over the NP surface was observed under TEM and slightly larger particle size (ca. 151 nm) was detected by DLS, suggesting the successful membrane coating. Zeta potential analysis indicated that the positively charged NP became negative after coating, largely owing to the charge screening by the membrane (Fig. 2B). It is well documented that the inflammation induces leukocyte homing and macrophage accumulation within inflammatory tissues (27, 28). There are several mediators promoting the macrophage chemotaxis (29), and recent investigations reported that cell membrane proteins, such as receptor proteins, play an important role in cell functions, such as inflammatory homing (30) and anti-inflammatory effects (31). The MM could direct coated nanoparticles to the inflammatory lesion by virtue

of CCR2 protein through chemokine-chemokine receptor axis, whereas TNFR2 proteins bind to tumor necrosis factor- $\alpha$  (TNF- $\alpha$ ) to alleviate inflammatory symptoms (32). To confirm whether the membrane proteins were still reserved after the extrusion, the total proteins of the MM, as indicated by SDS-polyacrylamide gel electrophoresis, were examined. As shown in Fig. 2C, the protein profiles from PPMM were almost identical to that of the native MM, which are different from that of the macrophage cell lysate (MCL; cytoplasm proteins that did not include cell membrane proteins) or CT26 cell membranes (CT26 CM). Western blotting results, as shown in Fig. 2D, suggested that the key proteins from MM, including CCR2 and TNFR2, were well reserved after the membrane coating.

Gel retardation assay indicated that plasmid encoding Cas9 could be completely inhibited at the N/P ratio of 2, suggesting good

ability of PBAE to complex large plasmid DNA (Fig. 2E). Note that the membrane coating did not affect the complexation ability of PPMM as compared with the uncoated NP complexes (Fig. 2F), although the surface zeta potential turned from positive to negative after coating. Furthermore, to anchor TMP into the membrane, a ROS-responsive molecule (termed BAM-TK-TMP) was synthesized by conjugating oleyl ether–modified poly(ethylene glycol) (OE-PEG) with TMP through a thioketal linker (TK). The synthesis procedures of BAM-TK-TMP are shown in fig. S5. Briefly, OE-PEG was first conjugated with the one carboxyl end of the ROS-responsive thioketal linker through a dicyclohexylcarbodiimide (DCC)–mediated coupling reaction to obtain the intermediate BAM-TK-COOH. Then, after TMP was converted to the phenolic form at its *para*-position, the other carboxyl end of BAM-TK-COOH was further added to TMP through the similar DCC-coupling reaction to obtain the final product BAM-TK-TMP. The chemical structures of synthesized molecules were characterized by proton nuclear magnetic resonance ( $^1\text{H}$  NMR). The disappearance of the proton signal at 3.75 ppm (parts per million) that belongs to the methoxy protons at *para*-position of benzene moieties proved the successful synthesis of TMP-OH (fig. S6). In comparison to the  $^1\text{H}$  NMR spectrum of OE-PEG (fig. S7), in the spectrum of BAM-TK-COOH (fig. S8), the proton signals between  $\delta$  2.7 and 2.9 ppm were attributed to PEG fragments. The proton signals at 2.6 to 3.0 ppm (peaks a and b) were assigned to the methylene protons in the vicinity of thioketal bonds, suggesting the successful introduction of the ROS-responsive linker. In the spectrum of BAM-TK-TMP (fig. S9), the newly formed characteristic peak at 6.5 ppm (peak b) was attributed to the methane protons in the benzene of TMP moieties, and the additional singlet at 3.81 ppm (peak c) was ascribed to the methoxy protons (33). Collectively, the information from  $^1\text{H}$  NMR spectra suggested that the proposed molecules were synthesized successfully. In addition, gel permeation chromatography (GPC) and matrix-assisted laser desorption/ionization time-of-flight (MALDI-TOF) results suggested that the synthesized polymers (including BAM-TK-TMP and PBAE) were in narrow distribution and high homogeneity (figs. S4 and S7 to S9). To investigate whether BAM-TK-TMP could be readily inserted into the membrane through its hydrophobic oleyl end, rhodamine-labeled OE-PEG was used to stain MM according to a previous report (34). As shown in fig. S10, strong red fluorescence could be observed over the macrophage surface, strongly suggesting the successful anchoring of OE-PEG–conjugated small molecules into the lipid membrane of macrophages. To further verify ROS-responsive cleavage of thioketal linkers to release TMP at the high ROS level (as shown in fig. S11), the released TMP from PPMMT nanoassemblies was monitored under the ROS-mimic environment. In the presence of 100  $\mu\text{M}$   $\text{H}_2\text{O}_2$  [the concentration relevant to *in vivo* condition (35)], whereas the release of TMP reached 16.8% in the first 24 hours and achieved 22.8% within 48 hours (Fig. 2G), the increase of  $\text{H}_2\text{O}_2$  concentration to 1 mM markedly promoted the total release of TMP up to 85% within 48 hours. However, without  $\text{H}_2\text{O}_2$  stimulation, the release of TMP from PPMMT was almost indiscernible due to the good chemical stability of thioketal linkers in the normal physiological condition. Together, these findings demonstrate that PPMMT nanoassemblies are successfully prepared and exhibit good sensitivity in response to ROS stimuli.

### Conditional activation of CRISPR-Cas9 by NanoProCas9 *in vitro*

To evaluate the transfection efficiency of PBAE, the transfection of plasmid encoding Cas9 with an enhanced green fluorescence protein

(EGFP) tag was carried out in CT26 cells (a *Mus musculus* colon carcinoma cell line), investigated with a fluorescence microscope, and quantified by flow cytometry (FCM). As indicated by strong green fluorescence in Fig. 3A, PBAE, PPMM, and PPMMT exhibited excellent ability to transfect CT26, and quantitative analysis performed by FCM indicated that EGFP-positive cells reached nearly 40% after 48 hours of transfection (Fig. 3B). PBAE displayed the comparable transfection efficiency as commercially available transfection agents, including jetPEI and Lipofectamine 3000, although the PBAE/plasmid complex coated with MM (PPMM) or PPMM anchored with BAM-TK-TMP (PPMMT) showed slightly declined transfection efficiency as compared with PBAE. To investigate the effects of ROS depletion by BAM-TK-TMP, we used 2,7-dichlorodihydrofluorescein diacetate (DCFH-DA) as a green fluorescent ROS probe to evaluate the depletion capability of ROS of BAM-TK-TMP. As a control, the treatment of CT26 with 100  $\mu\text{M}$   $\text{H}_2\text{O}_2$  showed the noticeable increase of fluorescence intensities, owing to the increased level of ROS species (Fig. 3, C and D). Nevertheless, the addition of BAM-TK-TMP could remarkably deplete ROS species in a concentration-dependent manner. On the basis of these results, we further transfected dsCas9 plasmid mediated by PPMMT to investigate the conditional activation of dsCas9 in response to ROS stimulation. To this end, the protein expression of FLAG-tagged Cas9 was investigated through Western blotting analysis. As expected, the protein band of wild-type Cas9 (166 kDa) was clearly observed after PPMMT-mediated transfection of plasmid encoding wild-type Cas9 (WT group) as shown in Fig. 3E, whereas it was hardly observed after PPMMT-mediated transfection of plasmid encoding dsCas9 without the  $\text{H}_2\text{O}_2$  stimulation (unstimulated group). In contrast, the band of dsCas9 (201 kDa) became visible after the stimulation (stimulated group), implying the stabilization of dsCas9 by released TMP (Fig. 3E). As shown in Fig. 3F, semiquantitative analysis of protein band intensities from Fig. 3E and fig. S12 indicated that the level of Cas9 protein in the stimulated group was approximately 80% relative to the wild-type group (WT group). In the meantime, real-time quantitative reverse transcription polymerase chain reaction (PCR) results suggested that there was almost no statistical difference between the unstimulated group and the stimulated group in terms of the Cas9 mRNA level, and similarly, no difference was observed between the stimulated group and the WT group. To further confirm that the degradation of dsCas9 is dependent on the pathway of ubiquitin-dependent proteasomal degradation, we used a proteasome inhibitor, MG132, to investigate whether such a degradation could be inhibited. By transfecting the plasmid encoding dsCas9 mediated by PPMM or PPMMT under the stimulation, the bands of the PPMM + MG132 group (with inhibitor) and the PPMMT group (with TMP stabilization) are clearly visible, in contrast with the PPMM group (without TMP stabilization and inhibitor) and the negative control group (untreated cells) (Fig. 3G). The above results suggested that stimuli-induced stabilization of dsCas9 is posttranslational, the process of which was not affected at the transcriptional level. In comparison with transcriptional control of CRISPR-Cas9, such as by light, the chemical control by means of stimuli-responsive activation of small molecules, in collaboration with the delivery technologies, offers a more straightforward way to improve the temporal specificity of CRISPR-Cas9. We further investigated the disruption of target genome loci by PPMMT-mediated transfection *in vitro*. Prolyl hydroxylase domain 2 (*PHD2*) gene is selected as the target of interest, as its down-regulation contributes to hypoxia-inducible

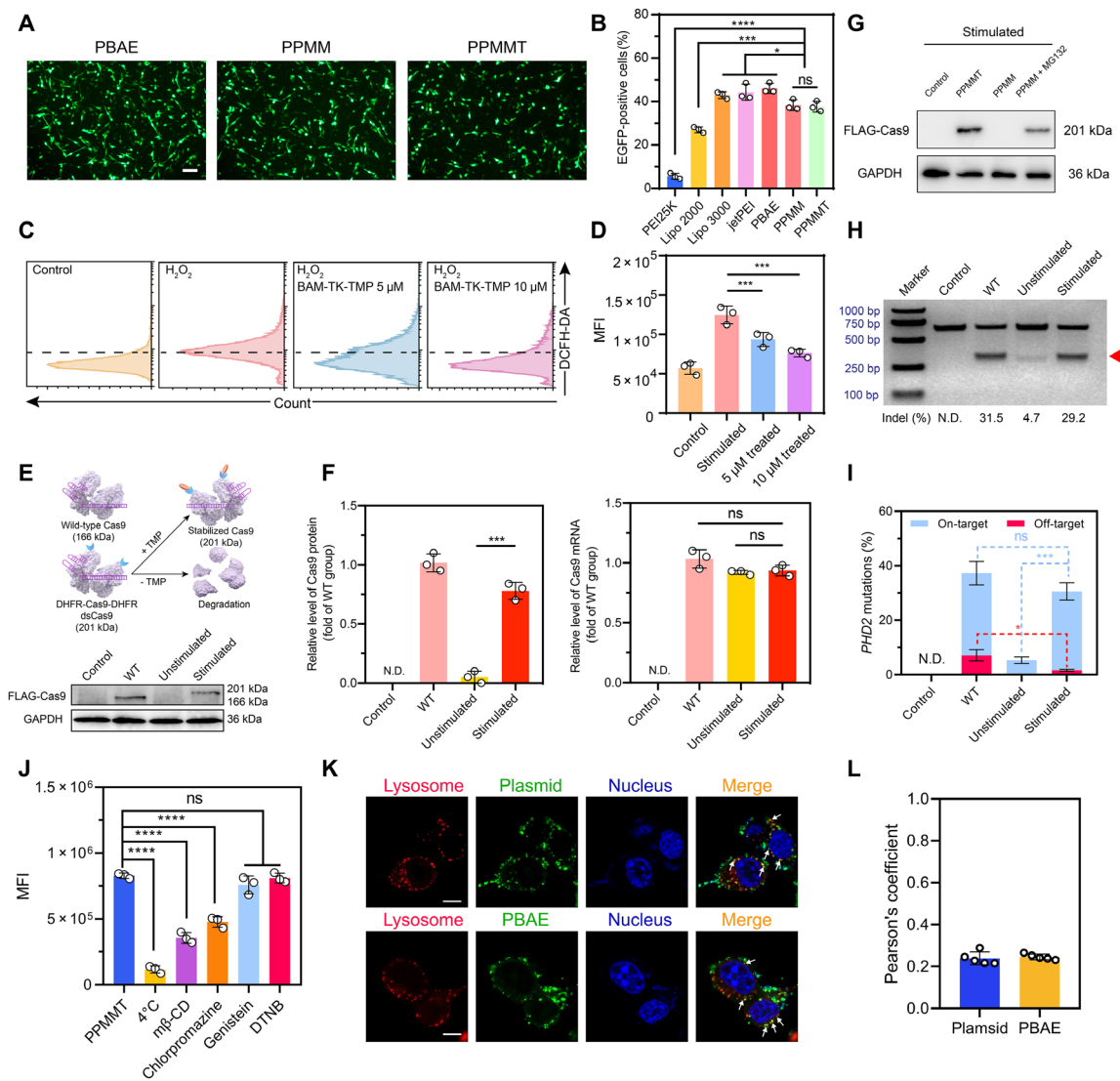


**Fig. 3. Intracellular delivery and conditional activation of genome editing mediated by NanoProCas9 in vitro.** (A) Fluorescence images of CT26 cells transfected with nanoparticles. Scale bar, 100  $\mu$ m. (B) Quantitative analysis of EGFP-positive cells by FCM. (C and D) Mean fluorescence intensity (MFI) of DCFH-DA in CT26 cells after the indicated treatment as investigated by FCM. (E) Schematic illustration of the stabilization of dsCas9 in the presence of TMP (top) and Western blotting analysis of Cas9 expression after PPMMT-mediated transfection (bottom). (F) Relative level of Cas9 protein (left) or mRNA (right) after PPMMT-mediated transfection. CT26 cells were used as the control group, and PPMMT-mediated transfection of plasmid encoding wild-type Cas9 was used as the WT group. (G) Expression level of Cas9 protein after treatment with MG132 proteasome inhibitor. (H) T7E1 indel analysis of *PHD2* locus of CT26 cells after PPMMT-mediated transfection of plasmid encoding wild-type Cas9 or dsCas9 targeting *PHD2* locus. (I) Deep sequencing result of mutation frequency on *PHD2* locus and off-target loci of CT26 cells with indicated treatment. (J) Investigation of cellular uptake mechanism of PPMMT in CT26 analyzed quantitatively by FCM. (K) Cellular uptake and endosomal escape of PPMMT in CT26 cells 6 hours after the transfection, as evaluated by confocal laser scanning microscopy (CLSM). Scale bar, 20  $\mu$ m. (L) Statistics of Pearson's correlation coefficient from CLSM images. Data represent means  $\pm$  SD;  $n = 3$  (B, D, F, I, and J) or  $n = 5$  (L). N.D., not detectable. The statistical significance is analyzed by one-way ANOVA with a Tukey post hoc test, \* $P < 0.05$ , \*\*\* $P < 0.001$ , and \*\*\*\* $P < 0.0001$ . ns, no significance.

factor-1 $\alpha$  (HIF-1 $\alpha$ ) stabilization, which further decreases the expression of TNF- $\alpha$  proinflammatory cytokines and relieves the inflammation (36). By optimizing sgRNA sequences (tables S1 and S2), we obtained optimal sgRNA sequence that was subsequently used to target *PHD2* locus (fig. S14). As shown in Fig. 3H, the delivery of PPMMT nanoassemblies without H<sub>2</sub>O<sub>2</sub> treatment displayed the faint disruption of *PHD2* locus, as revealed by the cleaved band produced by T7 endonuclease I (T7E1) digestion. In sharp contrast, the cleaved bands became clearly visible after H<sub>2</sub>O<sub>2</sub> treatment, suggesting the strong genomic disruption of *PHD2*. The

insertion and deletion (indel) frequency reached 29.2% under the stimulation, which is close to wild-type Cas9-induced genomic mutation (WT group in Fig. 3H and fig. S15) at *PHD2* locus. The degree of indel frequency agrees with Western blotting results, where the protein level of *PHD2* became the lowest under the stimulation and is close to that of wild-type Cas9 (fig. S16). Furthermore, we also investigated the activity of dsCas9 after PPMMT-mediated transfection with or without stimulation at different time points in the presence of 10% fetal bovine serum (FBS). As shown in fig. S17, the indel frequency first increased with time, reaching the highest at

48 hours after transfection. Subsequently, the indel frequency slightly dropped with time. In the meantime, we found that the background indel frequency (unstimulated/stimulated at the same time point) showed the similar trend but much lower value, suggesting the low background activity of dsCas9 at the unstimulated state under the serum condition. Collectively, the above results suggest that dsCas9 only can become stabilized and functional in the presence of its precursory stabilizer under ROS stimulation.

It was reported that prolonged expression of Cas9 would cause undesirable off-target effects, which may lead to potential catastrophic biological events, such as chromosomal translocations (37). Off-target effect is often observed in an elevated Cas9 activity, and the continuous, sustained expression of Cas9 can often result in off-target activity, which often occurs at a rate slower than that of on-target activity (8, 38, 39). To analyze the off-target effects in *PHD2* loci, Cas-OFFinder was used to estimate the off-target genomic loci and the corresponding primers for PCR were designed (tables S3 and S4). Deep sequencing was performed to quantitatively analyze the genomic mutations in both on-target and off-target sites following the treatment of NanoProCas9 (Fig. 3I). Whereas detectable off-target mutations (7.1%) were found following the transfection of wild-type Cas9, very low degree of off-target editing was observed in the NanoProCas9 group after the stimulation (1.6%). The specificity ratio, defined as the ratio of on-target mutations to off-target mutations (8), was ca.  $18.21 \pm 1.32$  in the NanoProCas9 group, which was much higher than that after the transfection of wild-type Cas9 ( $4.33 \pm 0.21$ ). As dsCas9 in NanoProCas9 is a Cas9 variant fused with structurally unstable protein domain derived from *Escherichia coli* DHFR, it is prone to rapid, ubiquitin-dependent proteasomal degradation without the stabilizer (12). Thus, upon the successful intracellular delivery of NanoProCas9, the nuclease only becomes functional when dsCas9 is stabilized by TMP. Previous reports have proved that the proteasomal degradation and nuclease activity of dsCas9 act in a concentration-dependent manner, where sufficient TMP concentration is required to recover the full nuclease activity of dsCas9 (11). Furthermore, given the fact that the restriction of the nuclease activity to a narrow temporal window is highly desirable to minimize the off-target events, we believe that the lower off-target activity contributed by NanoProCas9, as opposed to wild-type Cas9, is mainly due to the exhaustion of TMP released from NanoProCas9 that further results in the confined time window of genome-editing activity. Together, the delivery of NanoProCas9 may minimize off-target effects at the genomic level via conditional activation of dsCas9 endonuclease.

### Cellular uptake and endosomal escape capability of PPMMT nanoassembly

To investigate the endocytosis pathway of PPMMT, different inhibitors were supplemented before the transfection of the plasmid labeled by YOYO-1 (green fluorescence). CT26 cells were pretreated with different inhibitors to investigate their internalization pathway, and results are shown in Fig. 4J. First, we found that the uptake of PPMMT was significantly inhibited at 4°C, suggesting that the internalization is energy dependent. Second, the addition of chlorpromazine (an inhibitor of clathrin-mediated endocytosis) or methyl- $\beta$ -cyclodextrin (m $\beta$ -CD; a lipid raft inhibitor) could remarkably inhibit the internalization, whereas genistein (an inhibitor of caveolae-mediated uptake) or 5,5'-dithiobis-2-nitrobenzoic acid (DTNB; an inhibitor of thiol-mediated translocation) treatment merely affected the

uptake of the PPMMT, indicating that the endocytosis of the PPMMT is clathrin and lipid raft dependent.

To investigate the endosomal escape, plasmid DNA, PBAE, and endo/lysosome were labeled with green (YOYO-1 for the plasmid, fluorescein isothiocyanate for PBAE) or red fluorescence dye (LysoTracker for endo/lysosomes). At the same time, cell nuclei were labeled with blue fluorescence dye. After 6 hours of transfection, although a small fraction of plasmid/PBAE complexes were still trapped in lysosome (white arrows), green fluorescence from PBAE/plasmid has already spread out from the red fluorescence, suggesting the escape of PBAE/plasmid complexes from the endo/lysosome compartments (Fig. 4K). The colocalization coefficient between lysosomes and plasmids was analyzed by ImageJ (with JACoP plugin). Pearson's coefficient between lysosomes and plasmids (or lysosomes/PBAE) is 0.218 (0.226), as shown in Fig. 4L, confirming the strong capacity of endosomal escape.

To investigate whether TMP could diffuse from the extracellular milieu into the intracellular cytoplasm, we first added PPMM into the cell culture. After the transfection for 6 hours, the cell culture medium was replaced with a new one, in which BAM-TK-TMP was added. Without the stimulation of H<sub>2</sub>O<sub>2</sub>, only faint cleaved band in *PHD2* locus was observed [PPMM + BAM-TK-TMP (-) group; fig. S18]. However, the release of free TMP from BAM-TK-TMP upon the H<sub>2</sub>O<sub>2</sub> stimulation [PPMM + BAM-TK-TMP (+) group; fig. S18] resulted in significant genomic disruption at *PHD2* locus. These results suggest that only free TMP released from its precursory molecule (BAM-TK-TMP) could readily diffuse into the cell culture to induce the stabilization of dsCas9.

### NanoProCas9 system-mediated inflammatory genome editing in vivo

To evaluate the conditional activation in vivo, NanoProCas9 targeting *PHD2* gene in the inflammatory lesions was administered to the BALB/c mice with dextran sulfate sodium (DSS)-induced colitis (40, 41) (Fig. 4A), and mice without DSS or other treatments were set as the normal group. First, we studied the homing capacity of NanoProCas9 to the inflammatory lesions in vivo. As shown in fig. S19, 1,1'-diiodo-3,3',3'-tetramethylindocarbocyanine perchlorate (DiI)-labeled PPMMT could primarily accumulate in the colon of the DSS mice 24 hours after the systemic administration. In contrast, nanoassemblies were readily trapped by the macrophages in the mononuclear phagocyte system (MPS) of the healthy mice and tended to accumulate primarily in the liver, spleen, and lungs (42). To further investigate the therapeutic potential of NanoProCas9 in DSS-treated mice, the intravenous administration of PPMMT nanoassemblies was carried out. NanoProCas9-mediated therapy potently protected mice against DSS-induced shortening of colon and loss of body weight (Fig. 4, B to D). The disease activity index (DAI score, the measure of weight loss, stool consistency, and rectal bleeding) notably decreased after the treatment with PPMMT nanoassemblies, whereas the group treated with nanoassemblies without TMP (PPMM group) or PPMMT with plasmid encoding scrambled sgRNA (mock group) generally showed higher DAI score (Fig. 4E and fig. S20). The typical symptoms of colitis, including the loss of body weight and the decrease of colon length, were relieved in the PPMM or mock group, which is likely due to the binding of proinflammatory TNF- $\alpha$  by TNFR2, a receptor on the MM (32, 43). We further analyzed the indel frequency of *PHD2* locus of colon tissues by T7E1 assay. As shown in Fig. 4F, although

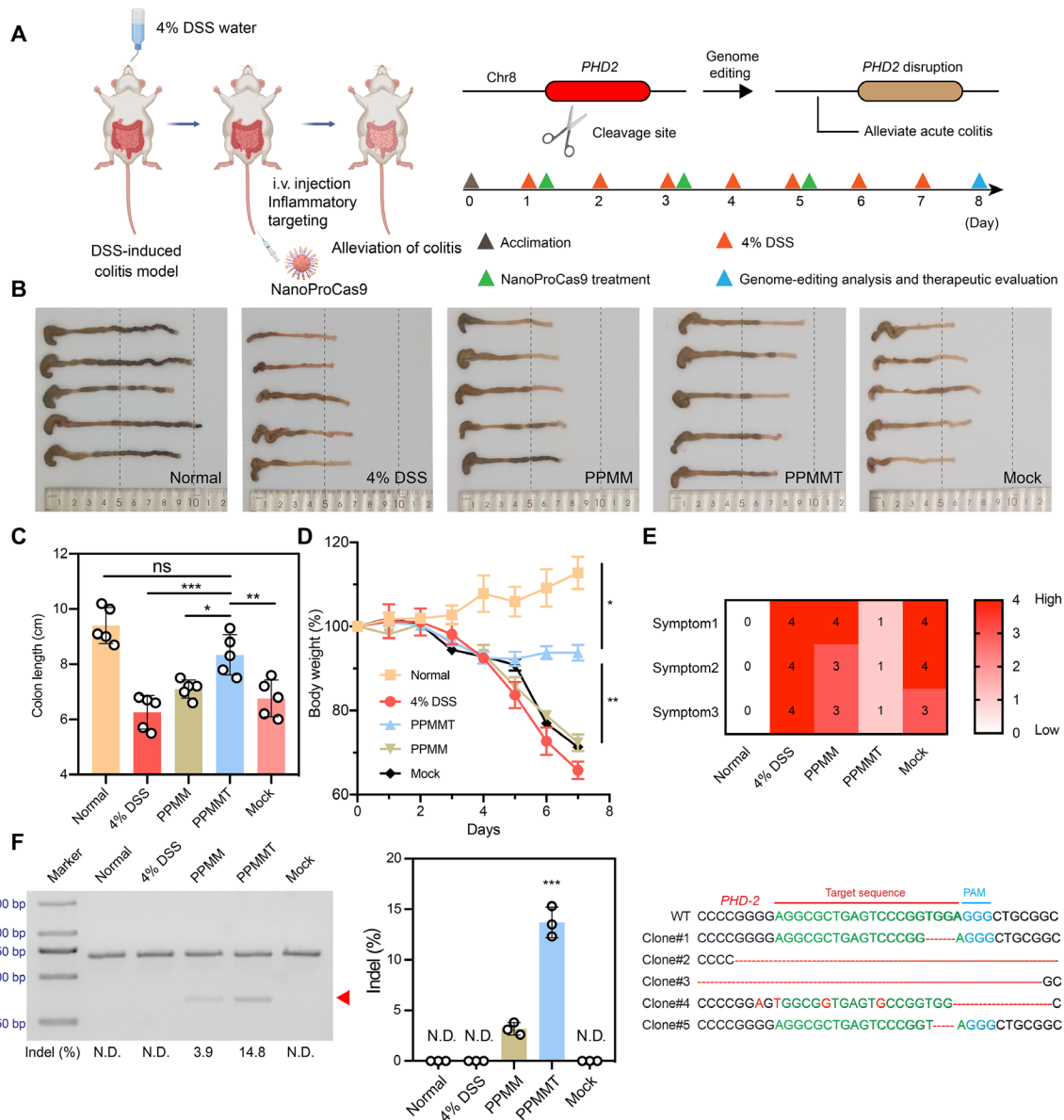


**Fig. 4. NanoProCas9-mediated inflammatory genome editing for the treatment of inflammatory bowel disease.** (A) Schematic illustration of colitis treatment with NanoProCas9. At day of 7, mice were sacrificed by cervical vertebra dislocation and colons were collected for further analysis. Mice without DSS or other treatments were set as the normal group. i.v., intravenous. (B) Colon images with a dotted line every 5 cm as a length indicator and (C) corresponding length after the indicated treatment. The data are shown as means  $\pm$  SD ( $n = 5$ ). One-way ANOVA with a Tukey post hoc test,  $*P < 0.05$ ,  $**P < 0.01$ , and  $***P < 0.001$ . (D) Changes in body weight of mice after the specified treatment. Data are normalized as a percentage of the body weight at day 0. Data are presented as means  $\pm$  SD ( $n = 5$ ). One-way ANOVA with a Tukey post hoc test,  $*P < 0.05$  and  $**P < 0.01$ . (E) DA I index of colitis of the indicated group. Symptom1, body weight; Symptom2, rectal bleeding; Symptom3, stool consistency. (F) Genomic disruption of *PHD2* after the indicated treatment as analyzed by T7E1 and Sanger sequencing of TA cloning; five sequences of clones with mutations are represented. Data are presented as means  $\pm$  SD ( $n = 3$ ). One-way ANOVA with a Tukey post hoc test,  $***P < 0.001$ . PAM, protospacer adjacent motif.

the faint band could be observed in the PPMM group due to the basal indel mutation, the PPMMT group showed an indel frequency of 14.8%, suggesting the successful genome editing of *PHD2*. Sanger sequencing confirmed the genome editing at the target loci, including base deletion and substitution around the protospacer adjacent motif.

Nonspecific genome editing at off-target tissues is one of the major concerns when genome editing was exploited for therapeutic purposes (44, 45). To evaluate the off-target editing at the tissue level,

we isolated heart, liver, spleen, lung, kidney, and colon from the mice after the treatment with PPMMs that contained plasmids encoding dsCas9 (PPMMT) or wild-type Cas9 (PPMMT-WT). T7E1 and deep sequencing analysis were presented to show the degree of the mutations at the target genomic locus in the major organs (fig. S21). Inspiringly, there were almost no distinct indel mutations detected in the major organs of the mice after treatment with PPMMT, while notable mutation in *PHD2* loci was observed in liver, lung,

and spleen of the mice with inflamed bowel after treatment with PPMMT-WT (Fig. 5A and figs. S22 and S23), causing undesired tissue off-target effects. As Kupffer cells in the liver are responsible for the binding and/or uptake of foreign materials, PPMMT nanoassemblies that were internalized by Kupffer cells during their circulation were likely to cause genome editing in the liver, leading to the high genome mutations in the liver in the PPMMT-WT group. Deep sequencing analysis also indicated that base deletion constituted the major type of mutation (10.60%), followed by substitution (3.91%) and insertion (1.14%) (fig. S24). At the mRNA level, there was a remarkable decline in terms of *PHD2* and *TNF- $\alpha$*  (Fig. 5, B and C).

The change of protein expression of *PHD2* and *TNF- $\alpha$*  was comparable to that of corresponding mRNA (Fig. 5, D and E, and fig. S25). While myeloperoxidase (MPO) activity was highly elevated in the colon of mice in the colitis group, it markedly decreased in the NanoProCas9-treated group (Fig. 5F). It was documented that the advance of colitis could lead to the sharp rise of white blood cells (WBCs) in the blood (41). As expected, the treatment by NanoProCas9 led to a sharp decrease in the WBC level, as compared with that in

the PPMMT or mock group (Fig. 5G). In addition, the functional damage of intestinal epithelial barriers is a characteristic feature of the intestinal injury. As suggested in Fig. 5H, PPMMT-treated DSS mice exhibited intestinal epithelial structures similar to those of the healthy mice. As a classical signal in the inflammatory diseases, the ROS level was also analyzed in virtue of red fluorescent probe. As shown in fig. S26, ROS species were abundant in the colon of DSS model, leading to the obvious damage of epithelial cells and chaos of gut immunity (40, 46). In contrast, PPMMT-treated mice showed ROS intensities in colon similar to those of the healthy mice. These results collectively suggested that the delivery of NanoProCas9 for the genome editing of *PHD2* gene is conducive to the treatment of colitis.

### Safety evaluation

We then evaluated the biocompatibility of NanoProCas9. First, cell counting kit-8 (CCK-8) and lactate dehydrogenase (LDH) release assays were performed to investigate the cell viability of the various components in NanoProCas9. The results showed that NP, MM, BAM-TK-TMP, and PPMMT (the concentration of each group was

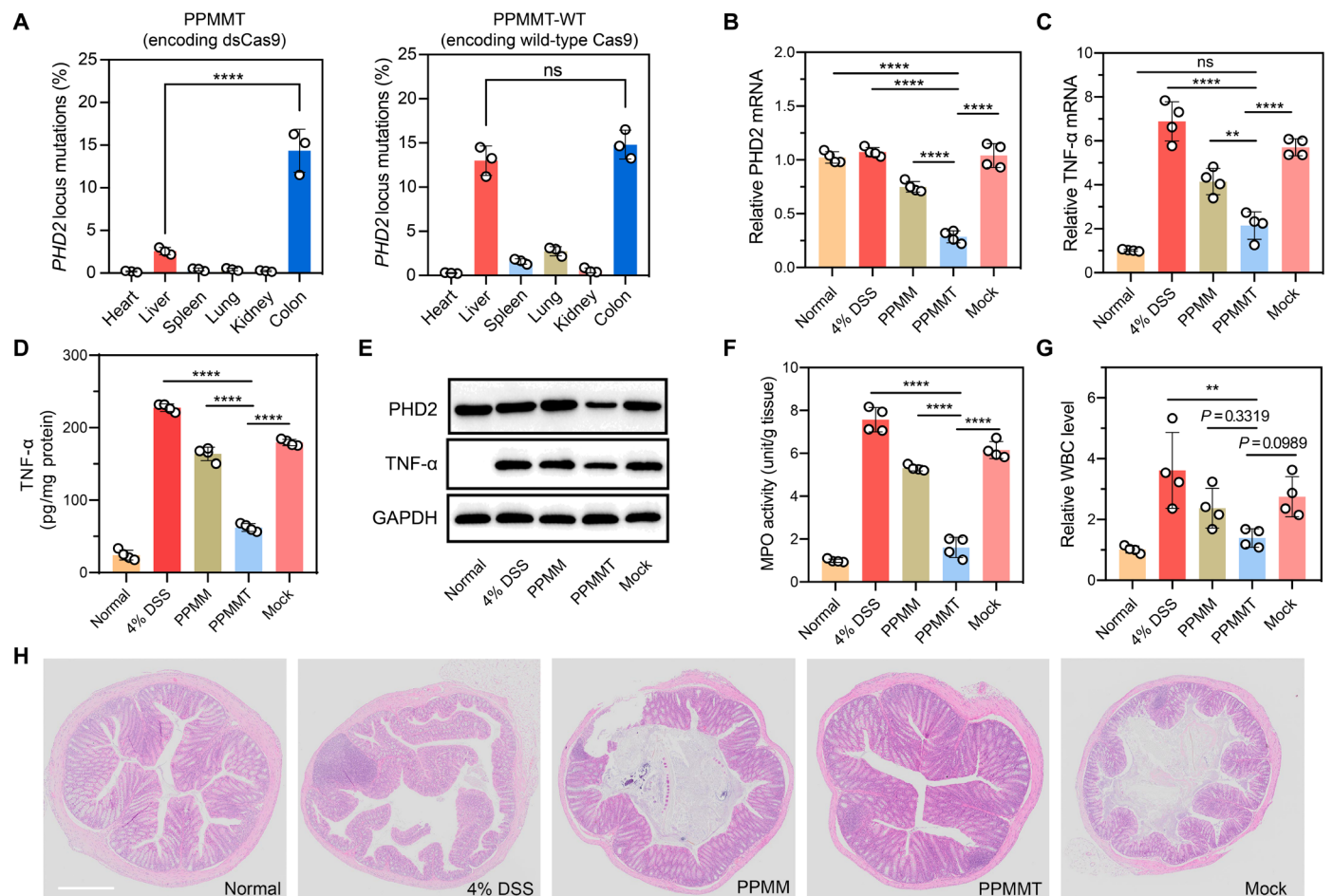


**Fig. 5. In vivo genome-editing specificity and pathological index.** (A) Deep sequencing results of *PHD2* mutation frequency in various organs after the treatment by PPMMT (with plasmid encoding dsCas9) or PPMMT-WT (with plasmid encoding wild-type Cas9). Data are presented as means  $\pm$  SD ( $n = 3$ ). One-way ANOVA with a Tukey post hoc test, \*\*\*\* $P < 0.0001$ . mRNA level of *PHD2* (B), mRNA level of *TNF- $\alpha$*  (C), and protein level of *TNF- $\alpha$*  analyzed by enzyme-linked immunosorbent assay (ELISA) (D), Western blotting analysis of *PHD2* and *TNF- $\alpha$*  expression (E), and MPO activity (F) in colon tissues. (G) Relative white blood cells in the blood after the indicated treatment. (H) Representative hematoxylin and eosin (H&E)-stained colon tissues in mice after the indicated treatment. Scale bar, 500  $\mu$ m. Data are presented as means  $\pm$  SD ( $n = 4$ ). One-way ANOVA with a Tukey post hoc test, \*\* $P < 0.01$  and \*\*\*\* $P < 0.0001$ .

equivalent to the final concentration of PPMPT) displayed low cytotoxicity and hardly affected the cell viability (fig. S27). In addition, to evaluate the safety of NanoProCas9 in vivo, the healthy mice were treated with NanoProCas9. No significant loss in body weight was observed for 8 days (fig. S28). Hematoxylin and eosin (H&E) staining of major organs (fig. S29) further revealed that there were no obvious pathological changes after the repeated administration of PPMPT, as compared with healthy control mice. Moreover, no abnormality was observed in terms of liver and kidney functions of the healthy mice after the treatment with NanoProCas9 (fig. S30).

## DISCUSSION

In this study, we developed a conditionally activatable CRISPR-Cas9 nanoassembly, which serves as prodrug for precise inflammatory genome editing. As a genome-editing prodrug, whereas dsCas9 is subjected to ubiquitin-dependent proteasomal degradation in non-specific tissues, it becomes stabilized and functional after being delivered to the inflammatory lesion, where the precursory small-molecule stabilizer can be released under the ROS stimuli to transform into its active form. The conditional activation by NanoProCas9 could afford deep-tissue genome editing, which well avoids previous challenges in the penetration depth that the optical regulation of CRISPR-Cas9 suffers. The MM not only plays an important role in directing NanoProCas9 to the inflammatory lesion but also serves as a supporter for anchoring small-molecule stabilizers. Thus, the systemic administration of NanoProCas9 enables the targeted delivery of dsCas9 plasmid into inflammatory lesions, where the precursory small molecule can be transformed into its active form under the ROS signals to stabilize expressed dsCas9. This also explains why NanoProCas9-mediated genome editing presents in a site-specific manner and can be activated exclusively in the inflammatory lesions.

A number of previous investigations suggest that MM-coated delivery vesicles could preferentially target inflammation lesions (32, 47); however, we still found that a large portion of these biomimetic nanoparticles were trapped by MPS in the liver (followed by lung and spleen) when the plasmid encoding wild-type Cas9 was delivered, causing considerable nontargeted, nonspecific genome editing at these organs. So far, several other effective approaches are reported to alleviate nonspecific genome editing in the liver. For example, Siegwart and coworkers reported a selective organ targeting (SORT) strategy by which lipid-based nanoparticles with the addition of a component (SORT molecule) can selectively deliver Cas9 mRNA to the target tissue, which represents an appealing way to minimize nonspecific editing in the liver (48, 49). Another possible strategy to avoid nonspecific editing in the liver is to express Cas9 with an inducible promoter, or a promoter that is active only in specific biological contexts (4). Unfortunately, the nonspecific genome editing in the liver is largely unexplored in these reported systems. In the current study, NanoProCas9, as a genome-editing prodrug system, can significantly decrease the nonspecific editing in the liver, with an indel frequency less than 3%. These encouraging results suggest that the NanoProCas9 system is generally inert in the liver despite its nonspecific distribution.

During our study, we did not observe the obvious side effects of local disruption of *PHD2* in the colon tissue. Although it was reported that systemic conditional knockout of *PHD2* in adult animals could induce angiogenesis, erythrocytosis, and changes in energy metabolism with ultimately lethal consequences (50), the

inflammation-specific genome editing mediated by NanoProCas9 can well evade the systemic disruption of *PHD2*, thereby greatly ensuring the safety profiles of genome editing at *PHD2* locus. Besides, owing to the restricted nuclease activity to a narrow temporal window, the conditional activation of genome editing mediated by NanoProCas9 also significantly reduces off-target mutations, which is similar to our previous findings and in agreement with other reports (8, 12). Regarding the clinical translation of NanoProCas9, the background activity of dsCas9 needs to be strictly limited. To address this issue, future efforts should be dedicated to screening different variants of dsCas9 by optimizing the number and position of DHFR domains in DHFR-fused Cas9 protein (11). Furthermore, the delivery of mRNA encoding dsCas9, instead of the plasmid form, may also contribute to lowering the background activity by shortening the time of dsCas9 expression (44). These strategies are expected to boost the safety profiles of NanoProCas9 that are considered for clinical translation.

In summary, as a proof-of-concept study, the NanoProCas9 system integrates targeted delivery and conditional activation of CRISPR-Cas9, offering a precise, site-specific therapeutic genome editing for inflammatory diseases. Such a system can avoid off-target mutations at nontargeted sites, thereby minimizing potential genotoxicity in those nonspecific tissues or organs. The NanoProCas9 system represents an innovative genome-editing prodrug and can be expanded to many other inflammatory diseases, such as lung/liver injury, atherosclerosis, and stroke. By virtue of similar engineering principles, such an inducible CRISPR system may also be tailored for the clinical scenarios where the epigenetic regulation or RNA editing is required in addition to genome editing. Collectively, the current study offers new insights for the rational design of CRISPR-Cas-based systems for safe, precise genome editing to accelerate the clinical translation. As a number of physiological and pathological signals, such as ATP, redox, and pH, can be leveraged to develop different types of genome-editing prodrugs, our current study opens a new avenue to precisely regulate CRISPR-Cas-based systems in vivo for more complicated and diverse genome-editing contexts.

## MATERIALS AND METHODS

### Materials

All reagents used in the experiments were purchased from commercial sources without further purification. Anhydrous dichloromethane (DCM), anhydrous *N,N*-dimethylformamide (DMF), HBr [48% (w/w) in H<sub>2</sub>O], DCC, 4-dimethylaminopyridine (DMAP), rhodamine B, dimethyl sulfoxide (DMSO), and TMP were purchased from Energy Chemical Co. Ltd. (Shanghai, China). Branched polyethyleneimine [PEI25K; weight-average molecular weight ( $M_w$ ): 25 kDa] was supplied by Meilunbio Co. Ltd. (Dalian, China). Dulbecco's modified Eagle's medium, RPMI 1640, and FBS were purchased from Sigma-Aldrich (USA). Lipofectamine 2000 and Lipofectamine 3000 transfection reagents were purchased from Thermo Fisher Scientific (Germany). The transfection reagent jetPEI was supplied by PolyPlus. The CCK-8 and LDH release assay kit were obtained from Beyotime Co. Ltd. (Shanghai, China). The dialysis bag [molecular weight cutoff (MWCO): 1000 Da] was obtained from Yuanye Bio-Technology Co. Ltd. (Shanghai, China). T7E1 enzyme was purchased from New England Biolabs (USA). Ultrapure water was obtained from a Milli-Q system. The plasmid encoding CMV-DHFR-Cas9-DHFR-U6-sgRNA (no. 85447) was supplied by Addgene.org, which was examined by Sanger sequencing and enzyme digestion.

CMVIE94-3XFLAG-NLS-Cas9-NLS-P2A-EGFP (CMV-Cas9-P2A-EGFP) and CMV-3XFLAG-NLS-Cas9-NLS (wild-type) were constructed in our laboratory. Target sgRNA (sg*PHD2*) was designed by online tools (<http://crispr.mit.edu/> and <http://chopchop.cbu.uib.no/>). All primers used in this work were listed in tables S1 to S5. The plasmids used in this work and corresponding nanocomplex information were listed in table S6 and in the “Plasmid information” section in Supplementary Materials. Primary antibodies used in this project included the following: Anti-TNF- $\alpha$  (1:1000) antibody was obtained from Beyotime (Shanghai, China). Anti-PHD2 (1:1000) antibody and cell/tissue lysis buffer [radioimmunoprecipitation assay (RIPA) buffer] were obtained from Solarbio Science and Technology (Beijing, China). Anti-FLAG antibody was obtained from HuaAn Biotechnology (HUABIO, Hangzhou, China). Anti-GAPDH (glyceraldehyde-3-phosphate dehydrogenase) antibody was obtained from Abcam (Shanghai, China). All enzyme-linked immunosorbent assay (ELISA) kits used in this project were supplied by Multisciences (Hangzhou, China). Cationic PBAE was synthesized according to the previous literature (scheme S1 and fig. S1) (16, 17).

### Characterization

The  $^1\text{H}$  NMR spectra and heteronuclear singular quantum correlation spectrum of PBAE were carried out on a Bruker 500-MHz NMR spectrometer and were reported as chemical shifts ( $\delta$ ) in ppm relative to tetramethylsilane ( $\delta = 0$ ). Proton spin multiplicities are reported as a singlet (s), doublet (d), triplet (t), quartet (q), and quintet (quint), with coupling constants (J) given in hertz, or multiplet (m). Mass spectra were recorded on a Shimadzu liquid chromatography–mass spectrometry (LC-MS) mass spectrometer (LC-MS 2020). TEM was carried out on a TEM (HT7700, Hitachi, Japan). Sizes and zeta potentials of the nanoparticles were characterized by Malvern Nano ZS90. Mass analysis of OE-PEG, BAM-TK-COOH, and BAM-TK-TMP was performed on MALDI-TOF (Ultraflextreme, Bruker, Germany). The molecular weight analysis of PBAE was performed on a Waters 1525/2414 GPC system. Confocal microscopy was performed on LSM-880 (Carl Zeiss, Germany). The DiI intensity was evaluated with an in vivo imaging system (IVIS Spectrum, PerkinElmer).

### Synthesis of 4-[(2,4-diaminopyrimidin-5-yl)methyl]-2,6-dimethoxyphenol (TMP-OH)

TMP-OH was synthesized according to the previous report (33). Briefly, TMP (1.00 g, 3.4 mmol) was dissolved in HBr (12.5 ml, 48% in  $\text{H}_2\text{O}$ ) and stirred at 95°C. After 20 min, the mixture was cooled down to room temperature and 2.97 ml of 50% (w/w) NaOH aqueous was added dropwise during stirring. After that, the solution was kept at 4°C overnight. The white precipitate was filtered and washed with double-distilled water ( $\text{ddH}_2\text{O}$ ). Residues were redissolved in boiling water, and 1 N NaOH was added to adjust pH to  $\sim 7.0$  for recrystallization. After being cooled down at 4°C for a while, a pink solid, TMP-OH, was precipitated and washed by water (630 mg, 66%).  $^1\text{H}$  NMR (DMSO-*d*<sub>6</sub>)  $\delta$  8.06 (s, -OH), 7.45 (s, 1H), 6.48 (s, 2H), 5.99 (s, -NH<sub>2</sub>), 5.63 (s, -NH<sub>2</sub>), 3.71 (s, 6H), and 3.47 (s, 2H). MS mass/charge ratio (*m/z*) found: 277.15, calculated: 277.12 for  $\text{C}_{13}\text{H}_{16}\text{N}_4\text{O}_3$  [ $\text{M}+\text{H}$ ]<sup>+</sup>.

### Synthesis of polyethylene glycol monooleyl ether-thioketal (BAM-TK-COOH)

To a solution of polyethylene glycol monooleyl ether ( $n = \sim 50$ , 250 mg, 0.1 mmol), DMAP (12 mg, 0.1 mmol) and thioketal (252 mg, 1 mmol) in 20 ml of anhydrous DCM at 0°C were added dropwise

with 10 ml of DCC (206 mg, 1 mmol)/DCM solution. After completion of addition of DCC, the reaction mixture was transferred to room temperature and stirred for 72 hours under a nitrogen atmosphere. After that, the insoluble by-product was filtered and the solvents were removed by rotary evaporation. The residue was dissolved in water and dialyzed (MWCO, 1000 Da) against water/methanol (1:1, v/v) for the first 24 hours and water for 48 hours. The product, BAM-TK, was collected and lyophilized for further reaction (193 mg, 70%).

### Synthesis of polyethylene glycol monooleyl ether-thioketal (BAM-TK-TMP)

TMP-OH (19 mg, 0.07 mmol) was added to a solution of BAM-TK (190 mg, 0.07 mmol) and DMAP (2 mg, 0.02 mmol) in 20 ml of anhydrous DMF. After stirring for 10 min under a nitrogen atmosphere, DCC (29 mg, 0.14 mmol), which was dissolved in 5 ml of DMF, was added dropwise into reaction mixture. After addition, the mixture was stirred at 30°C for 72 hours. The solvent of crude product was removed by rotary evaporation, and the product was redissolved in DCM. The by-product was filtered, and the filtrate was collected. After removal of DCM by rotary evaporation, the solid was redissolved in methanol. The product, BAM-TK-TMP, was obtained after dialysis against methanol for 24 hours and water for 48 hours (MWCO, 1000 Da) and further lyophilization.

### Deep sequencing assay

The schematic illustration of deep sequencing assay was shown in scheme S3. First, the off-target loci were evaluated and designed at CasOFFinder website ([www.rgenome.net/cas-offinder/](http://www.rgenome.net/cas-offinder/)). Subsequently, the fragments were amplified with corresponding primers, termed first PCR product. After purification by PCR/Gel Extraction and Purification kits (Vazyme Biotech Co., Ltd), the first PCR product was further amplified to obtain PCR fragments less than 250 base pairs (bp) containing corresponding gene loci. Then, the product, termed second PCR product, was further extracted and purified. After that, the second PCR product was amplified with primers containing index sequence and then purified by PCR/Gel Extraction and Purification kits. The products were sent to company for sequencing. The results were analyzed by CRISPResso2 according to the instruction (51).

### Statistical analysis

All data and figures in this paper were analyzed and plotted by GraphPad Prism 8.0. The obtained data are expressed as means  $\pm$  SD. Biological replicates were used in all experiments unless otherwise stated. The statistical significance was analyzed using one-way analysis of variance (ANOVA) with a Tukey post hoc test. *P* value less than 0.05 was considered significant (\**P* < 0.05, \*\**P* < 0.01, \*\*\**P* < 0.001, and \*\*\*\**P* < 0.0001). ns means no significance. N.D. refers to not detectable.

### SUPPLEMENTARY MATERIALS

Supplementary material for this article is available at <https://science.org/doi/10.1126/sciadv.abj0624>

### REFERENCES AND NOTES

1. C. Long, J. R. McAnally, J. M. Shelton, A. A. Mireault, R. Bassel-Duby, E. N. Olson, Prevention of muscular dystrophy in mice by CRISPR/Cas9-mediated editing of germline DNA. *Science* **345**, 1184–1188 (2014).
2. D. P. Dever, R. O. Bak, A. Reinisch, J. Camarena, G. Washington, C. E. Nicolas, M. Pavel-Dinu, N. Saxena, A. B. Wilkens, S. Mantri, N. Uchida, A. Hendel, A. Narla, R. Majeti,

- K. I. Weinberg, M. H. Porteus, CRISPR/Cas9  $\beta$ -globin gene targeting in human haematopoietic stem cells. *Nature* **539**, 384–389 (2016).
3. T. Wan, Q. Pan, Y. Ping, Microneedle-assisted genome editing: A transdermal strategy of targeting *NLRP3* by CRISPR-Cas9 for synergistic therapy of inflammatory skin disorders. *Sci. Adv.* **7**, eabe2888 (2021).
  4. Y.-L. Luo, C.-F. Xu, H.-J. Li, Z.-T. Cao, J. Liu, J.-L. Wang, X.-J. Du, X.-Z. Yang, Z. Gu, J. Wang, Macrophage-specific in vivo gene editing using cationic lipid-assisted polymeric nanoparticles. *ACS Nano* **12**, 994–1005 (2018).
  5. C. Xu, Z. Lu, Y. Luo, Y. Liu, Z. Cao, S. Shen, H. Li, J. Liu, K. Chen, Z. Chen, X. Yang, Z. Gu, J. Wang, Targeting of *NLRP3* inflammasome with gene editing for the amelioration of inflammatory diseases. *Nat. Commun.* **9**, 4092 (2018).
  6. W. L. Chew, M. Tabebordbar, J. K. W. Cheng, P. Mali, E. Y. Wu, A. H. M. Ng, K. Zhu, A. J. Wagers, G. M. Church, A multifunctional AAV-CRISPR-Cas9 and its host response. *Nat. Methods* **13**, 868–874 (2016).
  7. Y. Yu, X. Wu, N. Guan, J. Shao, H. Li, Y. Chen, Y. Ping, D. Li, H. Ye, Engineering a far-red light-activated split-Cas9 system for remote-controlled genome editing of internal organs and tumors. *Sci. Adv.* **6**, eabb1777 (2020).
  8. X. Chen, Y. Chen, H. Xin, T. Wan, Y. Ping, Near-infrared optogenetic engineering of photothermal nanoCRISPR for programmable genome editing. *Proc. Natl. Acad. Sci. U.S.A.* **117**, 2395–2405 (2020).
  9. Y. Nihongaki, T. Otake, M. Sato, Emerging approaches for spatiotemporal control of targeted genome with inducible CRISPR-Cas9. *Anal. Chem.* **90**, 429–439 (2018).
  10. Y. Chen, X. Yan, Y. Ping, Optical manipulation of CRISPR/Cas9 functions: From ultraviolet to near-infrared light. *ACS Mater. Lett.* **2**, 644–653 (2020).
  11. D. Manna, B. Maji, S. A. Gangopadhyay, K. J. Cox, Q. Zhou, B. K. Law, R. Mazitschek, A. Choudhary, A singular system with precise dosing and spatiotemporal control of CRISPR-Cas9. *Angew. Chem. Int. Ed.* **58**, 6285–6289 (2019).
  12. B. Maji, C. L. Moore, B. Zetsche, S. E. Volz, F. Zhang, M. D. Shoulders, A. Choudhary, Multidimensional chemical control of CRISPR-Cas9. *Nat. Chem. Biol.* **13**, 9–11 (2017).
  13. K. M. Davis, V. Pattanayak, D. B. Thompson, J. A. Zuris, D. R. Liu, Small molecule-triggered Cas9 protein with improved genome-editing specificity. *Nat. Chem. Biol.* **11**, 316–318 (2015).
  14. B. Zetsche, S. E. Volz, F. Zhang, A split-Cas9 architecture for inducible genome editing and transcription modulation. *Nat. Biotechnol.* **33**, 139–142 (2015).
  15. E. Blanco, H. Shen, M. Ferrari, Principles of nanoparticle design for overcoming biological barriers to drug delivery. *Nat. Biotechnol.* **33**, 941–951 (2015).
  16. A. K. Patel, J. C. Kaczmarek, S. Bose, A. J. Kauffman, F. Mir, M. W. Heartlein, F. DeRosa, R. Langer, D. G. Anderson, Inhaled nanoformulated mRNA polyplexes for protein production in lung epithelium. *Adv. Mater.* **31**, 1805116 (2019).
  17. S. Liu, Y. Gao, D. Zhou, M. Zeng, F. Alshehri, B. Newland, J. Lyu, J. O’Keeffe-Ahern, U. Greiser, T. Guo, F. Zhang, W. Wang, Highly branched poly( $\beta$ -amino ester) delivery of minicircle DNA for transfection of neurodegenerative disease related cells. *Nat. Commun.* **10**, 3307 (2019).
  18. E. L. Reichard, G. G. Chirico, W. J. Dewey, N. D. Nassif, K. E. Bard, N. E. Millas, D. A. Kraut, Substrate ubiquitination controls the unfolding ability of the proteasome. *J. Biol. Chem.* **291**, 18547–18561 (2016).
  19. X. Yang, Q. Tang, Y. Jiang, M. Zhang, M. Wang, L. Mao, Nanoscale ATP-responsive zeolitic imidazole framework-90 as a general platform for cytosolic protein delivery and genome editing. *J. Am. Chem. Soc.* **141**, 3782–3786 (2019).
  20. Q. Chen, G. Chen, J. Chen, J. Shen, X. Zhang, J. Wang, A. Chan, Z. Gu, Bioresponsive protein complex of aPD1 and aCD47 antibodies for enhanced immunotherapy. *Nano Lett.* **19**, 4879–4889 (2019).
  21. J. Liu, J. Chang, Y. Jiang, X. Meng, T. Sun, L. Mao, Q. Xu, M. Wang, Fast and efficient CRISPR/Cas9 genome editing in vivo enabled by bioreducible lipid and messenger RNA nanoparticles. *Adv. Mater.* **31**, 1902575 (2019).
  22. S. Nowag, R. Haag, pH-responsive micro- and nanocarrier systems. *Angew. Chem. Int. Ed.* **53**, 49–51 (2014).
  23. Q. Hu, P. S. Katti, Z. Gu, Enzyme-responsive nanomaterials for controlled drug delivery. *Nanoscale* **6**, 12273–12286 (2014).
  24. D. Zhou, L. Cutlar, Y. Gao, W. Wang, J. O’Keeffe-Ahern, S. McMahon, B. Duarte, F. Larcher, B. J. Rodriguez, U. Greiser, W. Wang, The transition from linear to highly branched poly( $\beta$ -amino ester)s: Branching matters for gene delivery. *Sci. Adv.* **2**, e1600102 (2016).
  25. L. Zhang, S. Deng, Y. Zhang, Q. Peng, H. Li, P. Wang, X. Fu, X. Lei, A. Qin, X. Yu, Homotypic targeting delivery of siRNA with artificial cancer cells. *Adv. Healthc. Mater.* **9**, e1900772 (2020).
  26. S. Shi, Y. Wang, B. Wang, Q. Chen, G. Wan, X. Yang, J. Zhang, L. Zhang, C. Li, Y. Wang, Homologous-targeting biomimetic nanoparticles for photothermal therapy and Nrf2-siRNA amplified photodynamic therapy against oral tongue squamous cell carcinoma. *Chem. Eng. J.* **388**, 124268 (2020).
  27. B. Meng, Y. Li, Y. Ding, X. Xu, L. Wang, B. Guo, B. Zhu, J. Zhang, L. Xiang, J. Dong, M. Liu, L. Xiang, G. Xiang, Myeloid-derived growth factor inhibits inflammation and alleviates endothelial injury and atherosclerosis in mice. *Sci. Adv.* **7**, eabe6903 (2021).
  28. Y. Oishi, I. Manabe, Macrophages in inflammation, repair and regeneration. *Int. Immunol.* **30**, 511–528 (2018).
  29. W. Xuan, Q. Qu, B. Zheng, S. Xiong, G.-H. Fan, The chemotaxis of M1 and M2 macrophages is regulated by different chemokines. *J. Leukoc. Biol.* **97**, 61–69 (2015).
  30. S. Willenborg, T. Lucas, G. van Loo, J. A. Knipper, T. Krieg, I. Haase, B. Brachvogel, M. Hammerschmidt, A. Nagy, N. Ferrara, M. Pasparakis, S. A. Eming, CCR2 recruits an inflammatory macrophage subpopulation critical for angiogenesis in tissue repair. *Blood* **120**, 613–625 (2012).
  31. G. Zhang, X. Li, Q. Liao, Y. Liu, K. Xi, W. Huang, X. Jia, Water-dispersible PEG-curcumin/amine-functionalized covalent organic framework nanocomposites as smart carriers for in vivo drug delivery. *Nat. Commun.* **9**, 2785 (2018).
  32. C. Gao, Q. Huang, C. Liu, C. H. T. Kwong, L. Yue, J.-B. Wan, S. M. Y. Lee, R. Wang, Treatment of atherosclerosis by macrophage-biomimetic nanoparticles via targeted pharmacotherapy and sequestration of proinflammatory cytokines. *Nat. Commun.* **11**, 2622 (2020).
  33. M. A. Sellmyer, I. Lee, C. Hou, C.-C. Weng, S. Li, B. P. Lieberman, C. Zeng, D. A. Mankoff, R. H. Mach, Bacterial infection imaging with [<sup>18</sup>F]fluoropropyl-trimethoprim. *Proc. Natl. Acad. Sci. U.S.A.* **114**, 8372–8377 (2017).
  34. D. C. Church, J. K. Pokorski, Cell engineering with functional Poly(oxanorbornene) block copolymers. *Angew. Chem. Int. Ed.* **59**, 11379–11383 (2020).
  35. X. Zhang, W. Wang, L. Su, X. Ge, J. Ye, C. Zhao, Y. He, H. Yang, J. Song, H. Duan, Plasmonic-fluorescent janus Ag/Ag<sub>2</sub>S nanoparticles for in situ H<sub>2</sub>O<sub>2</sub> activated NIR-II fluorescence imaging. *Nano Lett.* **21**, 2625–2633 (2021).
  36. E. Brown, C. T. Taylor, Hypoxia-sensitive pathways in intestinal inflammation. *J. Physiol.* **596**, 2985–2989 (2018).
  37. S. Q. Tsai, J. K. Joung, Defining and improving the genome-wide specificities of CRISPR-Cas9 nucleases. *Nat. Rev. Genet.* **17**, 300–312 (2016).
  38. J. Shin, F. Jiang, J.-J. Liu, N. L. Bray, B. J. Rauch, S. H. Baik, E. Nogales, J. Bondy-Denomy, J. E. Corn, J. A. Doudna, Disabling Cas9 by an anti-CRISPR DNA mimic. *Sci. Adv.* **3**, e1701620 (2017).
  39. S. Q. Tsai, Z. Zheng, N. T. Nguyen, M. Liebers, V. V. Topkar, V. Thapar, N. Wyvekens, C. Khayter, A. J. Iafrate, L. P. Le, M. J. Aryee, J. K. Joung, GUIDE-seq enables genome-wide profiling of off-target cleavage by CRISPR-Cas nucleases. *Nat. Biotechnol.* **33**, 187–197 (2015).
  40. Y. Lee, K. Sugihara, M. G. Gilliland III, S. Jon, N. Kamada, J. J. Moon, Hyaluronic acid-bilirubin nanomedicine for targeted modulation of dysregulated intestinal barrier, microbiome and immune responses in colitis. *Nat. Mater.* **19**, 118–126 (2020).
  41. W. Shen, Q. Wang, Y. Shen, X. Gao, L. Li, Y. Yan, H. Wang, Y. Cheng, Green tea catechin dramatically promotes RNAi mediated by low-molecular-weight polymers. *ACS Cent. Sci.* **4**, 1326–1333 (2018).
  42. Y.-N. Zhang, W. Poon, A. J. Tavares, I. D. McGilvray, W. C. W. Chan, Nanoparticle-liver interactions: Cellular uptake and hepatobiliary elimination. *J. Control. Release* **240**, 332–348 (2016).
  43. Q. Zhang, D. Dehaini, Y. Zhang, J. Zhou, X. Chen, L. Zhang, R. H. Fang, W. Gao, L. Zhang, Neutrophil membrane-coated nanoparticles inhibit synovial inflammation and alleviate joint damage in inflammatory arthritis. *Nat. Nanotechnol.* **13**, 1182–1190 (2018).
  44. J. A. Doudna, The promise and challenge of therapeutic genome editing. *Nature* **578**, 229–236 (2020).
  45. C.-F. Xu, G.-J. Chen, Y.-L. Luo, Y. Zhang, G. Zhao, Z.-D. Lu, A. Czarna, Z. Gu, J. Wang, Rational designs of in vivo CRISPR-Cas delivery systems. *Adv. Drug Deliv. Rev.* **168**, 3–29 (2021).
  46. Y. R. Na, M. Stakenborg, S. H. Seok, G. Matteoli, Macrophages in intestinal inflammation and resolution: A potential therapeutic target in IBD. *Nat. Rev. Gastroenterol. Hepatol.* **16**, 531–543 (2019).
  47. T. Sun, C. H. T. Kwong, C. Gao, J. Wei, L. Yue, J. Zhang, R. Dequan Ye, R. Wang, Amelioration of ulcerative colitis via inflammatory regulation by macrophage-biomimetic nanomedicine. *Theranostics* **10**, 10106–10119 (2020).
  48. J. B. Miller, P. Kos, V. Tieu, K. Zhou, D. J. Siegwart, Development of cationic quaternary ammonium sulfonamide amino lipids for nucleic acid delivery. *ACS Appl. Mater. Interfaces* **10**, 2302–2311 (2018).
  49. Q. Cheng, T. Wei, L. Farbiak, L. T. Johnson, S. A. Dilliard, D. J. Siegwart, Selective organ targeting (SORT) nanoparticles for tissue-specific mRNA delivery and CRISPR-Cas gene editing. *Nat. Nanotechnol.* **15**, 313–320 (2020).
  50. K. Takeda, A. Cowan, G.-H. Fong, Essential role for prolyl hydroxylase domain protein 2 in oxygen homeostasis of the adult vascular system. *Circulation* **116**, 774–781 (2007).
  51. K. Clement, H. Rees, M. C. Canver, J. M. Gehrke, R. Farouni, J. Y. Hsu, M. A. Cole, D. R. Liu, J. K. Joung, D. E. Bauer, L. Pinello, CRISPResso2 provides accurate and rapid genome editing sequence analysis. *Nat. Biotechnol.* **37**, 224–226 (2019).

**Acknowledgments:** We thank X. Chen, Y. Xue, and B. Li for help in this project. **Funding:** This work was supported by the National Natural Science Foundation of China (82073779 and 81872807), the Natural Science Foundation of Zhejiang Province (Distinguished Young Scholar

Program, LR21H300002), the Fundamental Research Funds for the Central Universities (2021XZZX036), the National Key Research and Development Program of China (2018YFA0901800), and the Leading Talent of "Ten Thousand Plan"—National High-Level Talents Special Support Plan. **Author contributions:** Y.P. conceived the project and designed experiments. X.Y. and Q.P. performed the experiments. H.X. constructed and verified the plasmids. Y.C. synthesized and characterized PBAE. X.Y. analyzed the data and wrote the manuscript. Y.P. supervised the project and wrote the manuscript. **Competing interests:** Y.P., X.Y., and Q.P. are named as inventors on pending patent, serial no. 202110969245.5, filed by China National Intellectual Property Administration on 23 August 2021. The authors declare no other

competing interests. **Data and materials availability:** All data needed to evaluate the conclusions in the paper are present in the paper and/or the Supplementary Materials. The deep-sequencing data generated in this paper are available in the NCBI Sequence Read Archive (Bioproject ID PRJNA768114). Source data are available in Zenodo (Record:5546124).

Submitted 21 April 2021

Accepted 21 October 2021

Published 8 December 2021

10.1126/sciadv.abj0624